Supplementary Information (SI) for Physical Chemistry Chemical Physics.

Supporting Information to

Discrepant lithium transference numbers due to heterogeneous speciation

Contents

Experimental Methods

1. Materials

Lithium difluorophosphate (Li[PO_2F_2], 99%), ethylene glycol dimethyl ether (monoglyme, 98%), diethylene glycol dimethyl ether (diglyme, 99%), triethylene glycol dimethyl ether (triglyme, 98%) and tetraethylene glycol dimethyl ether (tetraglyme, 98%) were obtained from Kishida Chemical Co., Ltd., Osaka, Japan.

Each electrolyte was prepared with Li[PO_2F_2] in the following salt:solvent molar ratio: 1:3 for monoglyme, 1:1.89 for diglyme, 1:1.33 for triglyme and 1:1 for tetraglyme, respectively inside a glovebox. The samples were stirred at 40°C until dissolution was complete, followed by addition of freshly cut lithium foil to check that no visible reaction occurs (gas evolution, blackening of the foil). The reference electrolyte for electrochemical measurements was prepared by dissolving 10.406 g Li[TfNTf] in 30.818 g triglyme inside a glovebox.

In some cases, a gel-like precipitate separated out during the preparation of the electrolytes, especially with G1 and G2 at higher concentrations of Li[PO_2F_2]. This observation was made with glyme and lithium salt samples from two independent manufacturers, one of which supplying battery-grade quality. ^{1}H, ^{13}C, ^{31}P, and ^{19}F NMR did not show a difference between solution and precipitate. For this reason, we could not prepare trustworthy samples with the composition corresponding to [Li(G1)$_{1.69}$][PO_2F_2], and decided to work with more dilute, but macroscopically homogeneous samples such as [Li(G1)$_3$][PO_2F_2]. It is worth noting that when [Li(G1)$_3$][PO_2F_2] was left to evaporate slowly, the gel-like precipitate was not observed, instead a solid residue was formed. This points towards the formation of crystalline solvates[1] in the Li[PO_2F_2]-glyme systems which is beyond the scope of this work (see also Figure S1).

2. Measurements

The thermal stability of the electrolytes was characterized by STA7200 Thermogravimetry/Differential Thermal Analyzer (Hitachi High-Tech Science Corporation). For the measurement, approximately 10 mg of the sample weighted into TGA open pans. The sample was then heated from 30 °C to 550 °C with a rate of 5 °C/min. In this study, the thermal decomposition temperature (T_d) was defined as the temperature of a 5% mass loss in the thermogravimetric curves.

The thermal transitions of investigated electrolytes were investigated by DSC7020 (Hitachi) equipped with liquid nitrogen cooling. The samples were hermetically sealed in aluminium pans in the glovebox. The sample pans were first heated to and kept at 80 °C for 10 min, followed by cooling to −100 °C, and then heated from −150 to 70 °C at a scan rate of 10 °C min^{-1} under a nitrogen atmosphere. The glass transition temperature (T_g) was determined from the onset temperatures of the heating thermograms.

The experiments to determine ionic transport property of electrolytes (ionic conductivity, Li^+ transference number, the salt diffusion coefficients, and electrode potentials of $\mathrm{Li/Li}^+$) performed in this study were conducted in the same way as in our previous study.[2] In brief, the ionic conductivity was measured using the complex impedance method in the frequency range of 500 kHz to 1 Hz with 10 mV amplitude (VMP2, Princeton Applied Research) at 30 °C. Li^+ transference number determined by the potentiostatic polarization method ($t^{\mathrm{PP}}_{\Omega,\mathrm{Li}^+}$) was measured using symmetric Li-Li coin cell. Inside the coin cell, as a separator, a porous glass filter paper (Advantec, GA55, 17 mm in diameter) soaked in the 80 µL liquid electrolyte were inserted into two Li foil electrodes (Honjo Metal, 16 mm in diameter). The symmetric coin cells were assembled using a R2032-type coin cell kit (case, cap, gasket, spacer, wave washer, SUS316L stainless steel parts, provided by Hohsen). The coin cells were aged at 30 °C for 24 h before measurement and the measurements were performed using a ModuLab XM potentiostat (Solartron Analytical) according to our previous study. The salt diffusion coefficients (D_{salt}) were determined using the same Li symmetric coin cell according to the literature.[3] The temperature dependences of the viscosity and density were measured using SVM3000 (Anton Paar). Diffusion coefficients were measured at 30.0°C *via* NMR diffusometry on an ECX 400 spectrometer (JEOL) equipped with a diffusion probe head with maximum magnetic field gradient of 12 T/m using a pulsed field gradient stimulated echo (PFGSTE) pulse sequence with bipolar sine-shaped pulsed gradients. The experimental procedure for pulsed field gradient stimulated echo (PGSE-NMR) has been described in detail in a previous study.[2] An overview of the experimental results can be found in Table S1. Density and viscosity values are given in Table S2, self-diffusion coefficients and derived quantities are given in Table S3. The TGA results are shown in Figure S1.

Table S1: Overview of experimental results.

	density	m_{salt}	m_{solvent}	Concentration	Ratio	Conductivity	EMF
Unit	g/mL	g	g	mol/L	Solvent:salt	mS/cm	mV
$[\mathrm{Li(G1)_3}][\mathrm{PO_2F_2}]$	1.0375(8)	5.758	14.426	2.743(2)	2.9998(4)	0.48(1)	
$[\mathrm{Li(G1)_{2.8}}][\mathrm{PO_2F_2}]$	1.0537(8)	3.343	7.814	2.926(2)	2.7987(7)		
$[\mathrm{Li(G1)_{3.2}}][\mathrm{PO_2F_2}]$	1.0322(8)	2.925	7.817	2.605(2)	3.1999(9)		
$[\mathrm{Li(G4)_{0.9}}][\mathrm{PO_2F_2}]$	1.2256(8)	3.548	6.577	3.980(3)	0.8999(5)		-88.6(6)
$[\mathrm{Li(G4)_1}][\mathrm{PO_2F_2}]$	1.2078(8)	3.934	8.106	3.657(3)	1.0003(5)	0.0390(1)	-96.5(6)
$[\mathrm{Li(G4)_{1.1}}][\mathrm{PO_2F_2}]$	1.1926(8)	3.942	8.937	3.383(2)	1.1006(6)		-104.6(4)

Table S2: Temperature dependent values for density and viscosity.

Temperature / °C	Density / g mL			Viscosity / cP		
	$[Li(G4)][PO_2F_2]$	$[Li(G1)_3][PO_2F_2]$	$[Li(G3)_{1.33}][PO_2F_2]$	$[Li(G4)][PO_2F_2]$	$[Li(G1)_3][PO_2F_2]$	$[Li(G3)_{1.33}][PO_2F_2]$
10	1.2266	1.0595	1.1926	716	5.36	161
20	1.2171	1.0485	1.1831	377	4.33	83.4
25	1.2124	1.0431	1.1784	283	3.92	79.0
30	1.2078	1.0376	1.1736	217	3.56	64.1
40	1.1987	1.0267	1.1642	134	2.97	43.9
50	1.1896	1.0155	1.1547	87.0	2.40	31.2
60	1.1805	1.0042	1.1453	59.3	2.00	23.0
70	1.1714	0.9921	1.1358	42.1	1.71	17.5
80	1.1624		1.1264	30.8		13.6

Table S3: Self diffusion coefficients in m^2/s as well as derived quantities.

	$[Li(G4)][PO_2F_2]$		$[Li(G1)_3][PO_2F_2]$	$[Li(G3)_{1.33}][PO_2F_2]$
^1H	1.82E-11	1.78E-11	8.05E-10	5.51E-11
^7Li	2.76E-12	2.65E-12	1.02E-10	8.06E-12
^{19}F	2.60E-12	2.52E-12	9.83E-10	8.04E-12
Λ_M^{NE} / Sm^2/mol	1.98E-05	1.91E-05	7.40E-04	5.95E-06
σNE / mS/cm	0.724	0.698	20.3	0.202
"ionicity"	5.4%	5.6%	2.4%	4.0%

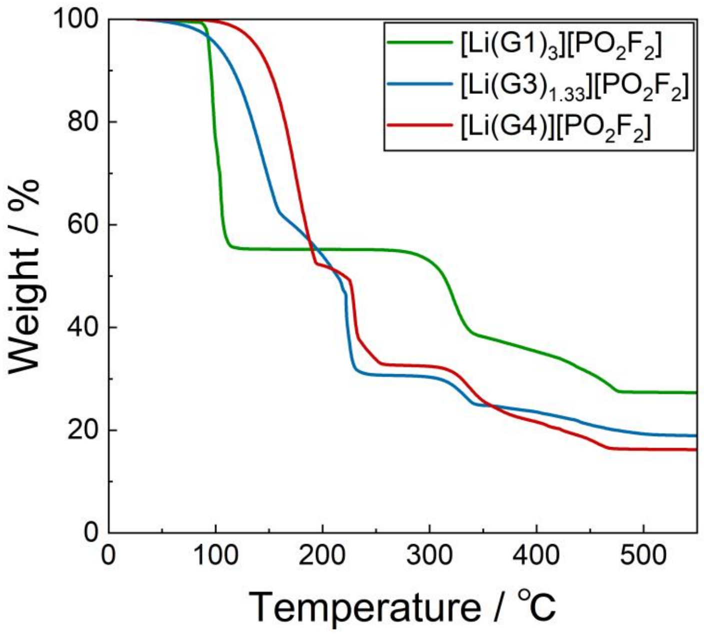

Figure S1: TGA traces for the glyme-$Li[PO_2F_2]$ systems.

3. Electrophoretic NMR

Electrophoretic NMR experiments were conducted on an *Avance Neo* or an *Avance III HD* 400 MHz spectrometer (*Bruker*, Rheinstetten, Germany) with a broadband gradient probehead (DiffBBO) capable of a maximum gradient strength of 17 T/m. A heated air stream of 300 L/h was used to maintain a temperature of 30 °C which was calibrated by a Pt100 thermocouple (*Greisinger Electronics*, Regenstauf, Germany).

The electrophoretic mobility of the species Li+, anion and solvent was determined based on ^{7}Li, ^{19}F and ^{1}H eNMR, respectively by using a pulsed field gradient sequence, complemented by electric field pulses (Figure S2). The induced coherent flux of charged species in the electric field causes a phase shift ϕ of the respective NMR signal according to:

$$\phi = \gamma\ \delta\ g\ \Delta\ E\ \mu \tag{S1}$$

At that, γ is the gyromagnetic ratio, δ the gradient pulse duration, g the applied gradient strength, Δ the observation time and $\mu = v/E$ is the electrophoretic mobility with the drift velocity v. The electric field $E = U/d$ is defined by the voltage U and electrode distance d. Upon variation of the applied voltage in a series of spectra, the electrophoretic mobility can be obtained by analyzing the resulting phase shift.

For the eNMR experiments, two electric field pulses of opposite polarity but same duration and strength complemented a Double Stimulated Echo (DSTE) pulse sequence (Figure S2). The electric field was applied either by a self-built or commercially available power source (*P&L Scientific*, Lindingö, Sweden). At gradient pulse durations δ of 1 ms and strengths g of 90 to 1000 G/cm, the observation time Δ was set between 100 and 300 ms depending on the sample and measurement. To enable sufficient heat dissipation, a delay of at least 40 s was set between separate scans. NMR spectra were fitted with phase-sensitive Lorentzian profiles using a self-written software as described previously to obtain voltage-dependent phase shifts.[4] By applying a linear fit, electrophoretic mobilities were obtained as demonstrated for representative phase shifts in Figure S3 and Figure S4. For each electrophoretic mobility determined, multiple measurements were performed on at least 3 different sample fillings, yielding an averaged mobility.

To apply voltage pulses of up to ±150 V to the sample, a self-built sample holder made out of VESPEL® with two palladium electrodes in a distance of 2.2 cm was used. To suppress convectional flow, 60 polyimide coated glass capillaries were inserted between both electrodes. A detailed description of the employed setup can be found elsewhere.[5] For sample preparation, the sample holder was dried at 90°C and 10^{-6} hPa for several hours and inserted into a 5 mm NMR tube containing 350 µL of the liquid sample. Remaining gas bubbles were carefully removed prior to the measurement.

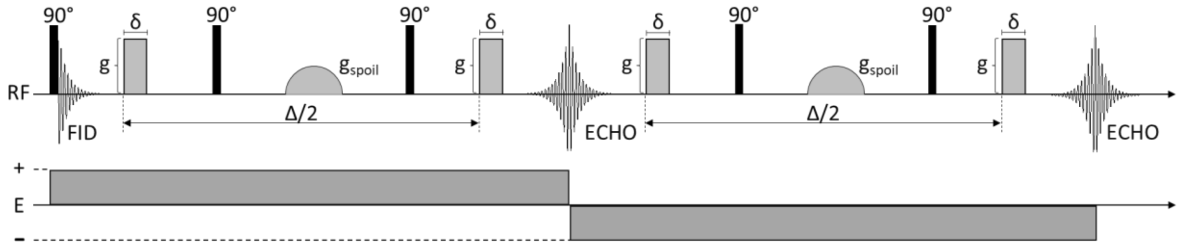

Figure S2: The Pulsed-Field Gradient Double Stimulated Echo (DSTE) pulse sequence accompanied by two electric field pulses as applied for electrophoretic NMR experiments.

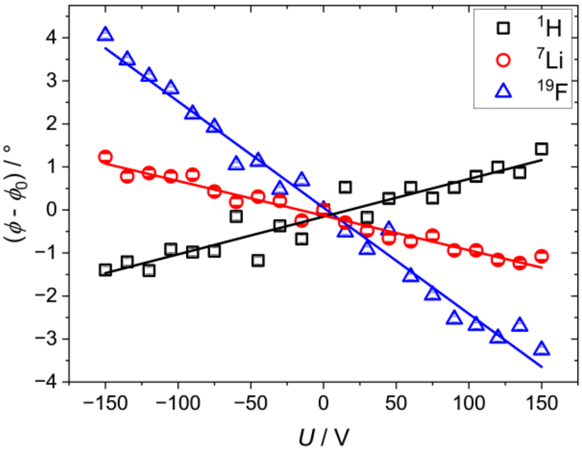

Figure S3: Representative voltage-dependent phase shifts (empty symbols) and linear fits (solid lines) of the ^{1}H, ^{7}Li and ^{19}F nuclei in the $[Li(G1)_3][PO_2F_2]$ electrolyte. As evident by a negative slope of the ^{7}Li phase shift, lithium cations drift towards the positive electrode.

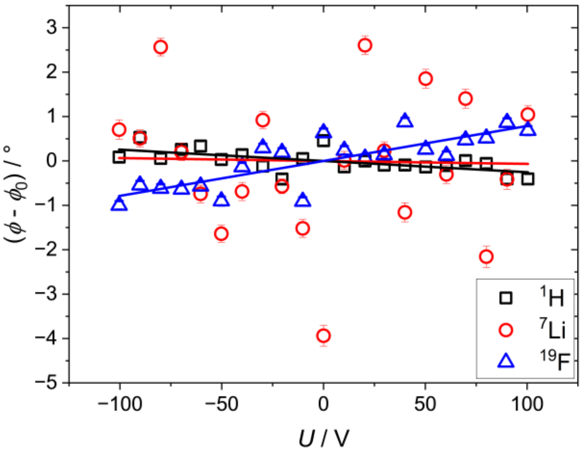

Figure S4: Representative voltage-dependent phase shifts (empty symbols) and linear fits (solid lines) of the ^{1}H, ^{7}Li and ^{19}F nuclei in the $[Li(G4)_1][PO_2F_2]$ electrolyte. All species show very low mobilities as observable by a small phase shift of the NMR signal. As a consequence, electrophoretic mobilities of the ^{7}Li nuclei turned out to be zero.

Computational Methods

4. Molecular Dynamics Simulations

MD simulations were performed in the NPT (equilibration run) / NVT (production run) ensemble using the in-house software: MPDynPFF program.[6] For the NPT ensemble, the system temperature and pressure were maintained at 363 K and 0.1 MPa using a Nosé–Hoover chain thermostat[7–9] and an Andersen barostat,[10] respectively, and time constants for the thermostat and the barostat were set at 0.5 ps and 2 ps, respectively.

For the NVT ensemble, the system temperature and volume/density were maintained at 363 K and 40.09 nm^3/1.045 g cm^{-3} (that was obtained by the equilibration run) using the same thermostat as the NPT ensemble. All C–H bonds were held rigid using the SHAKE/RATTLE algorithm,[11] and the reversible RESPA was employed for the multiple time step integration of the equations representing the motion of atoms.[12,13] The Lennard-Jones interaction was truncated at 12 Å, while long-range electrostatic and induced polarization interactions were estimated using the Ewald method.[14] Pair nonbonded interactions between atoms separated by one or two bonds were not considered (scaled with 0.0), while 1-4 interactions (atoms separated by three bonds) were scaled with 0.5.[15,16] The time step size for updating electrostatic interactions in the Ewald reciprocal space was 8 fs, while that for the other interactions was 2 fs. Periodic boundary conditions were employed for all three dimensions.

The preparation of the initial structure was carried out by following steps to reduce any biases arising from the initial arrangement of molecules. The system was initially allowed to evolve at 453 K and 10 MPa under the NPT ensemble from the low-density condition of the initial cubic box size (i.e., ~31 nm side length) for 50 ps, and was subsequently equilibrated at 453 K and 0.1 MPa for 1 ns. After this process, 40 ns equilibration MD runs were carried out at 363 K without changing the pressure, and an additional 1 ns equilibration run was done under the NVT ensemble. Finally, 40 ns production run was performed under the NVT ensemble collecting the trajectory data at 0.2 ps intervals for analysis. The number of molecules in a cubic cell was Li[DFP]/G1 = 70/210.

For the purpose of these simulations, the OPLS–AA-based polarizable force field was employed, as described in our previous report,[2,17,18] and in Table S4 to Table S7 and Figure S5.

5. Force field parameters

The force field parameters were modified to reproduce the MP2(full)/aug-cc-pVTZ level optimized molecular structures and binding energies of the Li^+ based on the OPLS-based parameters obtained from literatures[2,19] and the *ab initio* calculations. Atomic charges were determined based on the atomic charges obtained by electrostatic potential fitting[20,21] from the MP2(full)/aug-cc-pVTZ wave functions.

The total potential was defined by the following equation and more detailed information is available in our previous literature:[2]

$$\begin{aligned} U(\boldsymbol{r}^N) = {} & \sum_{i=1}^{N_{\text{bond}}} \frac{1}{2} k_b (r - r_0)^2 + \sum_{i=1}^{N_{\text{angle}}} \frac{1}{2} k_\theta (\theta - \theta_0)^2 + \sum_{i=1}^{N_{\text{torsion}}} \frac{1}{2} k_t (1 + \cos(n\varphi + \delta)) \\ & + \sum_{i=1}^{N} \sum_{j>i}^{N} 4\varepsilon \left\{ \left(\frac{\sigma}{r_{ij}} \right)^{12} - \left(\frac{\sigma}{r_{ij}} \right)^{6} \right\} + \sum_{i=1}^{N} \sum_{j>i}^{N} \frac{q_i q_j}{4\pi\varepsilon_0 r_{ij}} + U_{\text{ind}}(\boldsymbol{r}^N) \end{aligned} \tag{S2}$$

where the first three terms describe intramolecular interaction and last three terms describe the nonbond interaction, respectively. Here, k_b, k_θ and k_t are the force constants in each term, r_0 and θ_0 are the bond length and angle at the energy minimum, n is the number of waves, δ is the phase, ε is the potential depth at the minimum, σ is the distance at the potential is zero, ε_0 is the vacuum permittivity and q_i is the partial charge on *i*-th atom, respectively. The final term is the induction term, which is based on the isotropic atomic induced dipole model and described by the following equation.

$$U_{\text{ind}}(\boldsymbol{r}^N) = -\sum_{i=1}^{N} \mu_i \cdot E_i^0 - \frac{1}{2} \sum_{i=1}^{N} \sum_{j=1}^{N} \mu_i \cdot T_{ij} \cdot \mu_j + \sum_{i=1}^{N} \frac{\mu_i \cdot \mu_i}{2\alpha_i} \tag{S3}$$

μ_i ($= \alpha_i E_{\text{Total}}$) is the induced dipole moment, α_i is the isotropic atomic dipole polarizability of *i*-th atom. E_{Total} is the total electric field. E_i^0 is the electric field created by partial atomic charges, and T_{ij} is the second order dipole tensor.[2,17,18,22]

Table S4: Bond stretching parameters.

Bond	k_b / kcal mol^{-1} Å^{-2}	r_0 / Å
CG–CG	268.00	1.529
CG–HG	331.00	1.090
OG–CT	570.00	1.408
OG–CG	570.00	1.408
CT–HT	331.00	1.090
PD–OP	1540.24	1.494
PD–FP	860.92	1.607

Table S5: Angle bending parameters.

Angle	k_θ / kcal mol^{-1} rad^{-2}	θ_0 / deg.
OG–CT–HT	35.00	109.0
CG–CG–HG	37.43	110.7
CG–OG–CT	55.00	106.8
OG–CG–CG	80.00	109.0
OG–CG–HG	35.00	109.0
HG–CG–HG	33.00	107.8
HT–CT–HT	33.00	107.8
OP–PD–OP	205.61	126.85
OP–PD–FP	217.93	108.82
FP–PD–FP	239.16	96.08

Table S6: Torsional parameters.

Dihedral	k_t / kcal mol^{-1}			δ / degree
	$n = 1$	$n = 2$	$n = 3$	
CT–OG–CG–CG	−0.738	1.100	1.225	0.0
CT–OG–CG–HG	0.0	0.0	0.67	0.0
OG–CG–CG–OG	−0.563	3.114	2.181	13.57/−22.47/−27.78
HG–CG–CG–HG	0.0	0.0	0.318	0.0
HT–CT–OG–CG	0.0	0.0	0.67	0.0

Table S7: Nonbonding parameters.

Atom	σ / Å	ε / kcal mol^{-1}	α / a.u.
CT	3.50	0.066	9.000
CG	3.50	0.066	9.000
HT	2.50	0.030	2.000
HG	2.50	0.030	2.000
OG	2.98	0.144	7.000
LI	2.58	0.003	0.000
PD	3.70	0.200	24.000
FP	2.86	0.061	2.500
OP	3.20	0.150	5.000

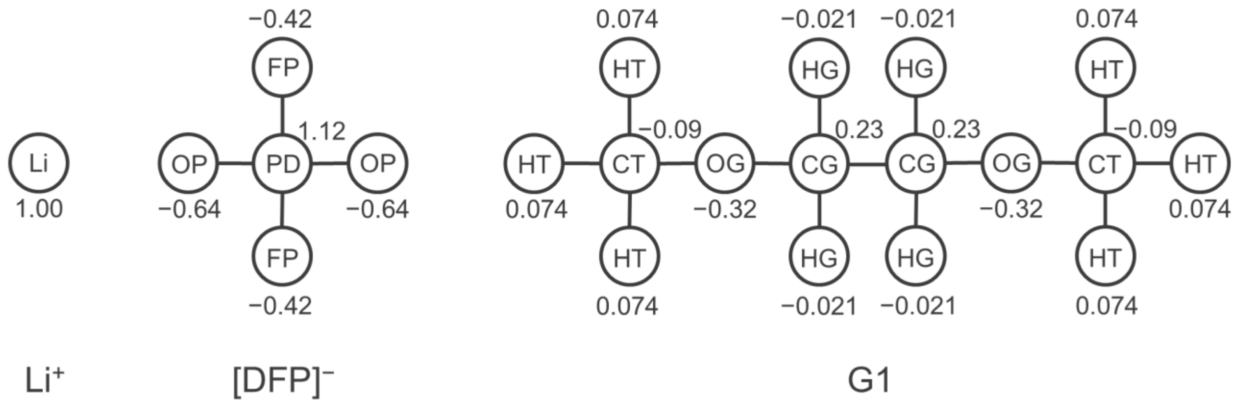

Figure S5: Atom types and atomic charges, q, of Li[DFP] and G1 used for the MD simulation.

6. Parameterisation of the $[PO_2F_2]^-$ anion

Bond stretching

The P–O and P–F bond stretching parameters were determined by fitting the MP2(full)/aug-cc-pVTZ level of theory energy with the harmonic potential, *cf*. Equation (S2) and Figure S6.

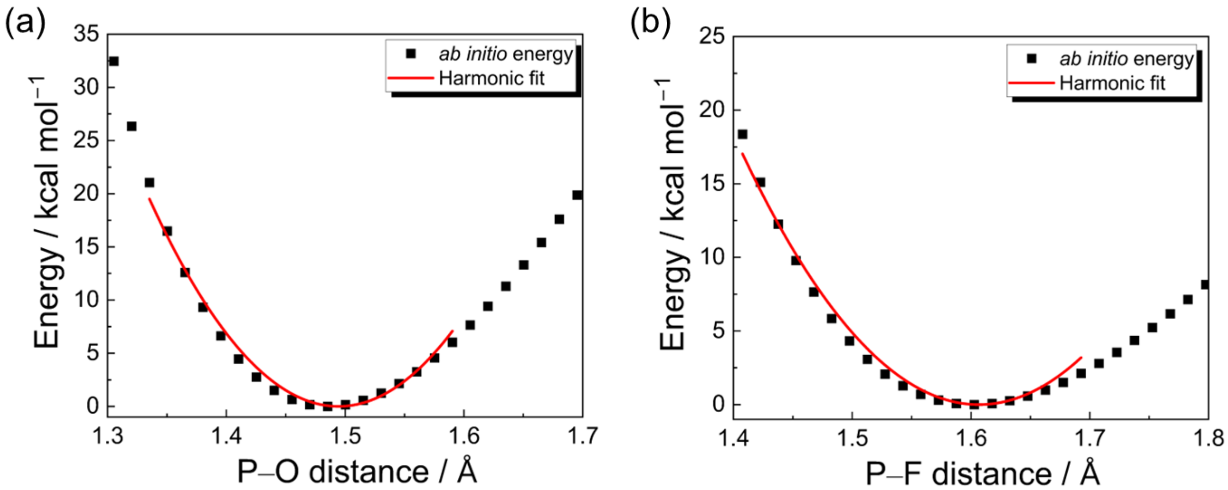

Figure S6: Harmonic fits of (a) P–O and (b) P–F bond stretching energies.

Angle bending

The O–P–O, O–P–F and F–P–F angle bending parameters were obtained by fitting the MP2(full)/aug-cc-pVTZ level of theory energy with the harmonic potential, *cf.* Equation (S2) and Figure S7.

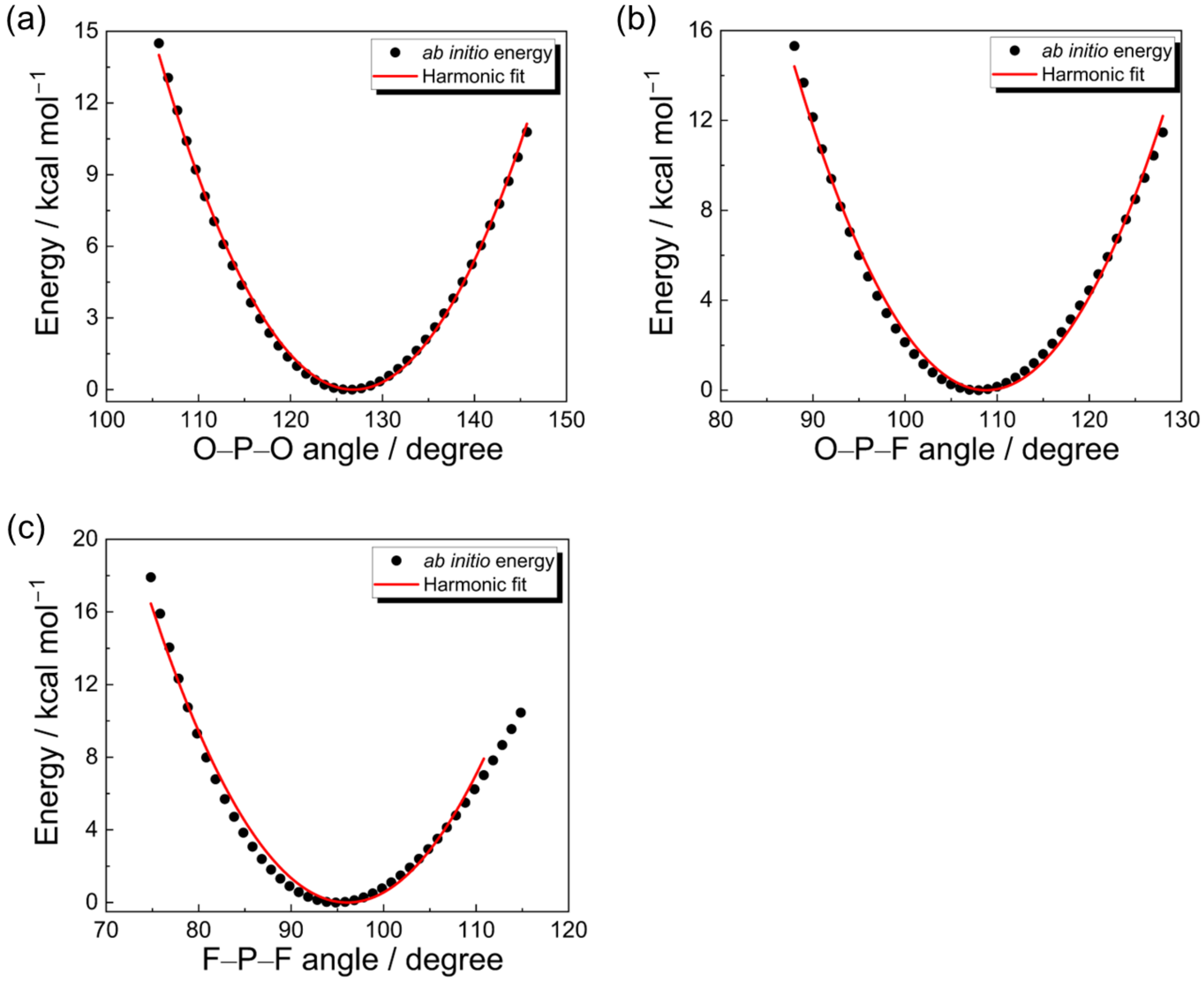

Figure S7: Harmonic fits of (a) O–P–O, (b) O–P–F and (c) F–P–F angle bending energies.

Stabilization energy of Li$^+$–[DFP]$^-$

Finally, all force field parameters were modified to reproduce the MP2(full)/aug-cc-pVTZ level optimized molecular structure and stabilization energy of the Li$^+$–[DFP]$^-$ pair as a function of distance between Li$^+$ and phosphorus atom in [DFP]$^-$ within ≈1 kcal mol^{-1}. Here, the value of the distance means the changes of the Li$^+$–P length based on the structure at the local minimum point.

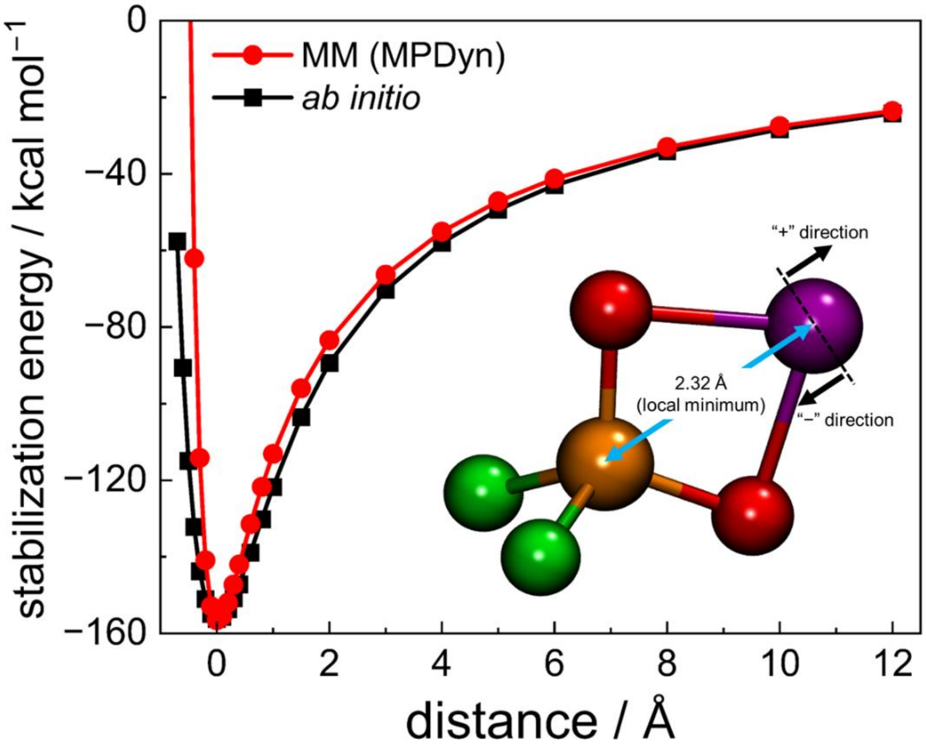

Figure S8: Stabilization energy in the Li$^+$–[DFP]$^-$ ion pair as a function of distance between Li$^+$ and phosphorus atom (Li: purple sphere, P: orange sphere, O: red sphere and F: green sphere in the CPK model in the insert). Here, the lithium ion coordinates the oxygen atoms.

7. Analysis of the coordination environments

The automatic analysis implemented in prealpha follows these main steps:

1) Select the atoms of interest. Here, Li, P, and O (only monoglyme-oxygen).
2) Group atoms as desired, in this case the two monoglyme oxygen atoms are treated as equivalent.
3) Define a cutoff distance as the minimum of the corresponding RDFs, see main manuscript.
4) The program then goes over all possible pairs of atoms through the simulation and collects those pairs which are within the cutoff distance, each of them considered as a connection.
5) For each acceptor (the discussion in the main manuscript focuses on Li^+), the program then keeps track of the connections to the surrounding donors and automatically tries to sort it into a list of existing species. If no entry is found, then a new species is made. Two species are considered the same if they have the same number and type of connections, and the same number of neighbouring molecules. 'type of connections' refers to molecule type (anion vs lithium vs glyme) and the atom group (here, G1-O, P and F).
6) After the whole trajectory has been analysed, the statistics are printed, such as how often a certain species is found, etc.
7) For each species, an intermittent time autocorrelation function is also printed.

The intermittent time autocorrelation function is calculated according to equation (S4)

$$C(t) = \frac{\langle (h(t_0 + t) - \langle h \rangle)(h(t_0) - \langle h \rangle) \rangle}{\langle (h(t_0) - \langle h \rangle)^2 \rangle} \tag{S4}$$

This function is evaluated separately for every observed species. For a given acceptor at a given point in time, the population variable h is either 1 (if the acceptor currently belongs to the species being evaluated) or 0 (if it belongs to any other species). The cornered brackets denote an ensemble average; *i.e.* an average over all molecular instances of the acceptor and over all possible starting timesteps t_0. Thus, $\langle h \rangle$ is the average occurrence / the probability of finding the evaluated species for this acceptor. Here, we need to acknowledge the similarity to the use of (S4) for hydrogen bond dynamics,[23–25] however unlike the latter, $\langle h \rangle$ does not approach 0 and thus the usual simplifications cannot be made here.

8. Heterogeneity and clustering

The α_2 parameter, defined in (S5), is a measure of deviation from normal (Gaussian) diffusion.

$$\alpha_2 = \frac{3\langle(\Delta r)^4\rangle}{5\langle(\Delta r)^2\rangle^2} - 1 \tag{S5}$$

Usually, deviations from 0 occur at intermediate timescales and are indicative of dynamical heterogeneity. Here, especially the G1 shows such a behaviour, Figure S9.

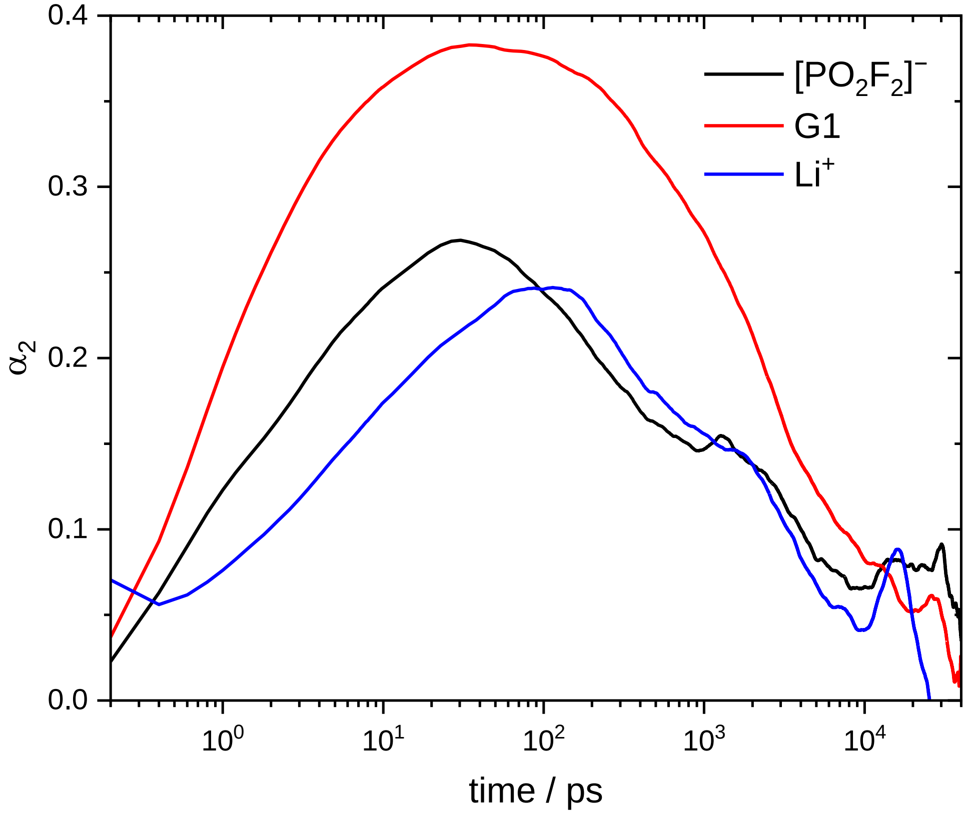

Figure S9: α_2 parameter for the simulation at 363 K.

In order to be able to calculate the volume fractions, we have obtained the mean volume from the radical Voronoi tessellation implemented in the TRAVIS software package, Table S1.

Table S8: Average molecular volumes obtained from the radical Voronoi tessellation.

Molecule	V / Å^3
$[PO_2F_2]^-$	86.3
G1	164.7
Li^+	21.1

Thus, we are able to calculate the volume fractions for the observed species, Table S9, using the following logic. For ease of understanding, we also provide a cross reference to the relevant raw data file in the directory “output-363K”.

- **$[Li(G1)_2]^+$**: Of the 70 lithium ions in the box, 28.2% belong to $[Li(G1)_2]^+$. In this case, species and coordination environment are the same because there is no communal solvation. There are twice as many G1 molecules belonging to this species.
  - ➔ All-to-Li_acceptor1_species_autocorrelation.dat as <h> of #2. Can also be found in All-to-Li_acceptor1_speciation_statistics_table.dat and All-to-Li_acceptor1_speciation_statistics.dat.
- **Ion pairs**: Of the 140 ions in the cluster analysis, at the cutoff distance, 9.1% were found in ion pairs, each with one lithium and one ion.
  - ➔ GLOBAL_cluster_statistics.dat, 2 members, weight_average=charge≈0
- **Free anions**: 8.0% of the 70 $[PO_2F_2]^-$ anions are not coordinated to lithium.
  - ➔ Li-to-All_acceptor1_speciation_statistics_table.dat
- **Free G1**: There are 210 G1 molecules in the box, of which statistically 53.8% are not coordinating any lithium.
  - ➔ Li-to-All_acceptor2_speciation_statistics_table.dat
- **Aggregates**: From the global cluster analysis results, the number of cations $\#\mathrm{Li}_i^+$ in each cluster with I members can be calculated by multiplying the atom_fraction with the number of atoms considered, in this case 140, and the fraction of Li^+ in that cluster, Equation (S6). $\#[\mathrm{PO_2F_2}]_i{}^-$ can then be calculated accordingly, (S7). The total numbers $\#Li^+$ and $\#[PO_2F_2]^-$ in the aggregates are then just the sum for all clusters with more than two members.

$$\#\mathrm{Li}_i^+ = \mathrm{atom\_fraction} \cdot 140 \cdot \frac{\mathrm{members} + \mathrm{weight\_average}}{2 \cdot \mathrm{members}} \tag{S6}$$

$$\#[\mathrm{PO_2F_2}]_i{}^- = \mathrm{atom\_fraction} \cdot 140 \cdot \frac{\mathrm{members} - \#\mathrm{Li}^+}{\mathrm{members}} \tag{S7}$$

➔ GLOBAL_cluster_statistics.dat

- The number of G1 molecules decorating the aggregates are calculated from the total number of glyme molecules (210) minus free G1 minus those G1 part of the species $[Li(G1)_2]^+$.

Table S9: Average content of relevant species in the simulation box and the corresponding volume of the species as the sum of its constituents, *cf*. Table S8.

Species	Average number in box			Resulting volume / Å^3			φ
	#Li^+	#$[PO_2F_2]^-$	#G1	Li^+	$[PO_2F_2]^-$	G1	
$[Li(G1)_2]^+$	19.74	0.00	39.48	416	0	6501	16%
ion pairs	6.37	6.37	0.00	134	549	0	1.6%
free anions	0.00	5.62	0.00	0	485	0	1.2%
free G1	0.00	0.00	112.88	0	0	18586	44%
aggregates	42.79	58.02	57.64	901	5005	9492	37%

For the sake of completeness, the resulting compositions in terms of molar (=number) fractions are given in Table S10.

Table S10: Composition of species normalized for each species and for each constituents.

Species	Distribution of constituents in each species (columns add to 100%)			Composition of each species in terms of constituents (rows add to 100%)		
	Li^+	$[PO_2F_2]^-$	G1	Li^+	$[PO_2F_2]^-$	G1
$[Li(G1)_2]^+$	28.7%	0.0%	18.8%	33.3%	0.0%	66.7%
ion pairs	9.2%	9.1%	0.0%	50.0%	50.0%	0.0%
free anions	0.0%	8.0%	0.0%	0.0%	100.0%	0.0%
free G1	0.0%	0.0%	53.8%	0.0%	0.0%	100.0%
aggregates	62.1%	82.9%	27.4%	27.0%	36.6%	36.4%

References

1 W. A. Henderson, *J. Phys. Chem. B*, 2006, **110**, 13177–13183.

2 F. Philippi, M. Middendorf, K. Shigenobu, Y. Matsuyama, O. Palumbo, D. Pugh, T. Sudoh, K. Dokko, M. Watanabe, M. Schönhoff, W. Shinoda and K. Ueno, *Chem. Sci.*, 2024, **15**, 7342–7358.

3 D. B. Shah, H. Q. Nguyen, L. S. Grundy, K. R. Olson, S. J. Mecham, J. M. DeSimone and N. P. Balsara, *Phys. Chem. Chem. Phys.*, 2019, **21**, 7857–7866.

4 F. Schmidt, A. Pugliese, C. C. Santini, F. Castiglione and M. Schönhoff, *Magn. Reson. Chem.*, 2020, **58**, 271–279.

5 M. Gouverneur, J. Kopp, L. van Wüllen and M. Schönhoff, *Phys. Chem. Chem. Phys.*, 2015, **17**, 30680–30686.

6 Shinoda, W. MPDynPFF, MPDyn for polarizable force field: Okayama, 2022, http://theocomp.chem.okayama-u.ac.jp/member/wshinoda/MPDyn2/

7 S. Nosé, *Mol. Phys.*, 1984, **52**, 255–268.

8 W. G. Hoover, *Phys. Rev. A*, 1985, **31**, 1695–1697.

9 G. J. Martyna, M. L. Klein and M. Tuckerman, *J. Chem. Phys.*, 1992, **97**, 2635–2643.

10 H. C. Andersen, *J. Chem. Phys.*, 1980, **72**, 2384–2393.

11 J.-P. Ryckaert, G. Ciccotti and H. J. C. Berendsen, *J. Comput. Phys.*, 1977, **23**, 327–341.

12 M. Tuckerman, B. J. Berne and G. J. Martyna, *J. Chem. Phys.*, 1992, **97**, 1990–2001.

13 G. J. Martyna, M. E. Tuckerman, D. J. Tobias and M. L. Klein, *Mol. Phys.*, 1996, **87**, 1117–1157.

14 M. P. Allen and D. J. Tildesley, *Computer Simulation of Liquids*, Oxford University Press, 2nd edn., 2017, vol. 1.

15 G. Kaminski and W. L. Jorgensen, *J. Phys. Chem.*, 1996, **100**, 18010–18013.

16 W. L. Jorgensen, D. S. Maxwell and J. Tirado-Rives, *J. Am. Chem. Soc.*, 1996, **118**, 11225–11236.

17 S. Ikeda, S. Tsuzuki, T. Sudoh, K. Shigenobu, K. Ueno, K. Dokko, M. Watanabe and W. Shinoda, *J. Phys. Chem. C*, 2023, **127**, 13837–13845.

18 K. Shigenobu, S. Tsuzuki, F. Philippi, T. Sudoh, Y. Ugata, K. Dokko, M. Watanabe, K. Ueno and W. Shinoda, *J. Phys. Chem. B*, 2023, **127**, 10422–10433.

19 S. Tsuzuki, W. Shinoda, M. Matsugami, Y. Umebayashi, K. Ueno, T. Mandai, S. Seki, K. Dokko and M. Watanabe, *Phys. Chem. Chem. Phys.*, 2015, **17**, 126–129.

20 U. C. Singh and P. A. Kollman, *J. Comput. Chem.*, 1984, **5**, 129–145.

21 B. H. Besler, K. M. Merz and P. A. Kollman, *J. Comput. Chem.*, 1990, **11**, 431–439.

22 O. Borodin and G. D. Smith, *J. Phys. Chem. B*, 2006, **110**, 6279–6292.

23 M. Kohagen, M. Brehm, J. Thar, W. Zhao, F. Müller-Plathe, B. Kirchner, F. Müller-Plathe and B. Kirchner, *J. Phys. Chem. B*, 2011, **115**, 693–702.

24 S. Gehrke, M. von Domaros, R. Clark, O. Hollóczki, M. Brehm, T. Welton, A. Luzar and B. Kirchner, *Faraday Discuss.*, 2018, **206**, 219–245.

25 A. Luzar, *J. Chem. Phys.*, 2000, **113**, 10663–10675.